ADVANCED MATERIALS
www.advmat.de

Over 20% Efficient Water-Based Layer-by-Layer Organic Solar Cells with High Thickness Tolerance Enabled by Surfactant Promoted Electrostatic Interaction

Chen Xie, Xuanlin Wen, Hongjie Chen, Ting Xu,* Hansheng Chen, Yong Zhang, Lin Hu,* Lanxiang Yu, Siyue Zhou, Qing Yan, Haoxuan Zeng, Jinyang Dai, Jiale Li, Baoshen Deng, Hui Liu,* Zeguo Tang, Bin He, Peigang Han, Peng You, Guangye Zhang, Shunpu Li, and Yiwang Chen**

Aqueous processing represents a promising eco-friendly fabrication route for organic solar cells (OSCs), aligning with growing industrial sustainability requirements. While water-dispersed semiconducting nanoparticles (NPs) offer an attractive solution, the essential surfactants required for NP stabilization typically compromise device performance. In this study, surfactant-engineered donor NPs are systematically evaluated for constructing optimized active layers through a sequential layer-by-layer (LBL) deposition approach. The surfactant named sodium dodecyl phosphate (SDP), featuring dual anionic charges, generates exceptional electrostatic potential (ESP) differences that promote strong donor-acceptor interactions. This electrostatic engineering enables the formation of a pseudo-planar heterojunction structure (PPHJ) with ideal vertically graded morphologies in thick active layers. Therefore, the PM6:L8-BO binary OSC processed by mesostructured NP (mn)-LBL (SDP) strategy shows excellent thickness tolerance and achieved a PCE of 18.9% (certified as 18.3%) with a 300 nm active layer. Furthermore, the mn-LBL OSCs with the ternary PM6:L8-BO:BTP-eC9 deliver a champion PCE of 20.3% (certified as 19.9%) processed by a non-halogenated water/toluene solvent system. This work establishes a general surfactant selection paradigm that simultaneously addresses the conflicting demands of nanoparticle stabilization, morphological control, and device performance, paving the way for sustainable manufacturing of high-efficiency OSCs.

1. Introduction

The recent evolution of donor materials, non-fullerene acceptors (NFAs), and device architectures has elevated the power conversion efficiencies (PCEs) of single-junction organic solar cells (OSCs) beyond the 20% threshold.[1–6] his remarkable advancement has redirected research focus toward scalable manufacturing paradigms. However, the transition from laboratory-scale demonstrations to industrial production faces substantial technological barriers, particularly concerning the narrow optimal thickness window (100–120 nm) of the photoactive layer.[7–11] Although increased layer thickness theoretically improves photon harvesting, it concurrently introduces three critical challenges: i) compromised morphological stability, ii) insufficient exciton dissociation efficiency due to limited diffusion lengths, and iii) enhanced charge recombination losses from prolonged transport pathways.[12–14] Resolving this thickness-performance dichotomy represents a fundamental prerequisite for commercially viable OSC technologies.

Conventional bulk-heterojunction (BHJ) systems, fabricated through single-step donor:acceptor (D/A) blend casting (BC), inherently generate extensive interfacial domains for exciton separation.[15,16] Yet this approach fails to establish the graded vertical phase segregation essential for efficient charge extraction in thicker films.[17,18] The layer-by-layer (LBL) deposition methodology presents an alternative paradigm, enabling

C. Xie, X. Wen, H. Chen, H. Chen, L. Yu, S. Zhou, Q. Yan, H. Zeng, J. Dai, J. Li, B. Deng, H. Liu, Z. Tang, B. He, P. Han, P. You, G. Zhang, S. Li
College of New Materials and New Energies
Shenzhen Technology University
Shenzhen 518118, China
E-mail: xiechen@sztu.edu.cn; liuhui@sztu.edu.cn

The ORCID identification number(s) for the author(s) of this article can be found under https://doi.org/10.1002/adma.202508783

DOI: 10.1002/adma.202508783

Y. Chen
College of Chemistry and Chemical Engineering/Institute of Polymers and Energy Chemistry (IPEC)
Nanchang University
999 Xuefu Avenue, Nanchang 330031, China
E-mail: ywchen@ncu.edu.cn

L. Hu
College of Biological and Chemical Engineering
Jiaxing University
Jiaxing 314001, China
E-mail: hulin@zjxu.edu.cn

controlled vertical component stratification that aligns donor-rich and acceptor-rich regions with respective electrodes, enabling a so-called pseudo-planar heterojunction (PPHJ) structure.[19,20] Nevertheless, conventional LBL processing suffers from inadequate D/A interpenetration—a limitation that scales adversely with film thickness. Recent breakthroughs by Lai et al. established that amplified electrostatic potential (ESP) differentials between D/A components can overcome this interdiffusion barrier.[20,21] Our group previously addressed this challenge through the introduction of a mesostructured nanoparticle (mn) interlayer, which mediates molecular-scale mixing between sequentially deposited layers while maintaining advantageous vertical phase separation.[22,23] The resultant mn-LBL devices exhibited unprecedented thickness tolerance, preserving PCEs even at clinically relevant film dimensions.

In this work, we systematically investigate the previously overlooked role of residual nanoparticle surfactants in determining mn-LBL OSC performance—an inevitable consequence of colloidal stabilization requirements.[24,25] It is reported that the optimal surfactant for organic electronics processing must satisfy several critical criteria: 1) effective emulsion stabilization to synthesize monodisperse polymer semiconductor nanoparticles, 2) facilitating particle coalescence for the deposition of high-quality, smooth thin films with low roughness and high fill factors, 3) ensuring facile post-deposition removal of residual surfactants, and 4) promoting intra-particle polymer ordering.[26] Through comparative analysis of surfactants bearing diverse ionic functionalities, we identify that anionic headgroups significantly enhance ESP-mediated D/A interactions. Particularly, sodium dodecyl phosphate (SDP) demonstrates exceptional performance owing to its doubly charged molecular architecture, which generates superior electrostatic driving forces for interlayer diffusion. Detailed characterization reveals that SDP-modified systems achieve near-ideal D/A interpenetration while mitigating excessive vertical phase segregation—a critical advancement for thick-film processing. The optimized mn-LBL (SDP) devices processed via environmentally benign water/toluene solvents achieve remarkable efficiencies: ≈20.0% in binary PM6:L8-BO systems and 18.9% (certified 18.3%) at 300 nm active layer thickness—representing state-of-the-art performance for thick-film OSCs. Furthermore, extension to ternary PM6:L8-BO:BTP-eC9 systems yields a certified 20.3% (certified as 19.9%) PCE, validating the universal applicability of this approach. Therefore, we suggest the surfactant selection rule for processing mn-LBL OSCs with high performance by enhancement of electrostatic interaction. Beyond demonstrating aqueous-processable high-efficiency OSCs, this work establishes fundamental surfactant selection criteria based on electrostatic potential modulation, providing a new materials engineering dimension for LBL photovoltaic devices.

H. Liu
Quality and Standards Academy
Shenzhen Technology University
Shenzhen 518118, China

T. Xu
Institute of Technology for Future Industry
Shenzhen Institute of Information Technology
Shenzhen 518172, China
E-mail: xuting_robin@pku.edu.cn

Y. Zhang
Sustainable Energy and Environment Thrust
Function Hub
The Hong Kong University of Science and Technology (Guangzhou)
Nansha, Guangzhou, Guangdong 511453, China

2. Results and Discussion

The chemical structures of the active layer materials chosen for this work are illustrated in **Figure 1a**. Building upon our prior methodology, the mesostructured donor underlayer was fabricated through emulsion-based deposition of aqueous nanoparticle (NP) inks,[22] a technique successfully employed to water-process multiple high-performance optoelectronic devices.[27,28] Subjecting donor solutions to high-shear blending with aqueous media yielded stable oil-in-water emulsions (see Supporting Information). Amphiphilic surfactants were incorporated to prevent colloidal instability through dual suppression of flocculation and Ostwald ripening, resulting in monodisperse organic semiconductor NPs. As shown in Figure 1b, surfactants with various pendant groups were used for PM6 nanoparticle synthesis, including sodium dodecyl phosphate (SDP), sodium dodecyl sulfate (SDSO4), sodium dodecyl sulfonate (SDSO3), dodecyl trimethylammonium bromide (DTAB), dodecyl pyridinium bromide (DPB) and 1-dodecyl-3-methylimidazolium bromide (DMMB). As shown in Figure 1c, the NPs are homogenously dispersed and the average diameters are ≈60–150 nm for those systems with different surfactants (Figure 1d). In comparison with other counterparts, a slight absorption redshifts with an enhanced 0–0/0–1 peak ratio are observed in the NP dispersion containing SDP as surfactant, which is also observed in those of NP deposited films (Figure S1, Supporting Information), indicating a molecularly ordered structure in NPs.[29,30]

The density functional theory (DFT) calculation shows that the ESPs of surfactants are orders of magnitude greater than those of active layer materials (Table S1, Supporting Information). The ionic head groups induce significant ESP values and charge imbalances in surfactant molecules (Table S2, Supporting Information). Particularly noteworthy are the anionic surfactants (SDP, SDSO4, SDSO3), whose strong electronegativity creates substantial ESP differentials at D/A interfaces-a critical factor governing intermolecular interactions during LBL deposition.[31] Further analysis of molecular dipole moments demonstrates that SDP's unique doubly charged architecture generates a dipole moment much greater than single-charge surfactants (Figure S2, Supporting Information). Therefore, the PM6 NPs containing SDP are expected to formation of comparatively strong intermolecular interactions with the acceptor. Our modeling suggests these ESP characteristics directly influence vertical phase segregation in BHJ films, with greater surfactant ESP values correlating with more favorable D/A interpenetration profiles. As illustrated in Figure 1f, during mn-LBL processing, aqueous donor NP deposition creates a mesostructured template whose residual anionic surfactant moieties establish an ESP gradient. Subsequent acceptor solution deposition then exploits this pre-patterned electrostatic landscape, driving the formation of optimized vertical D/A distributions through controlled intermixing. This potential-driven assembly represents a significant advance over conventional

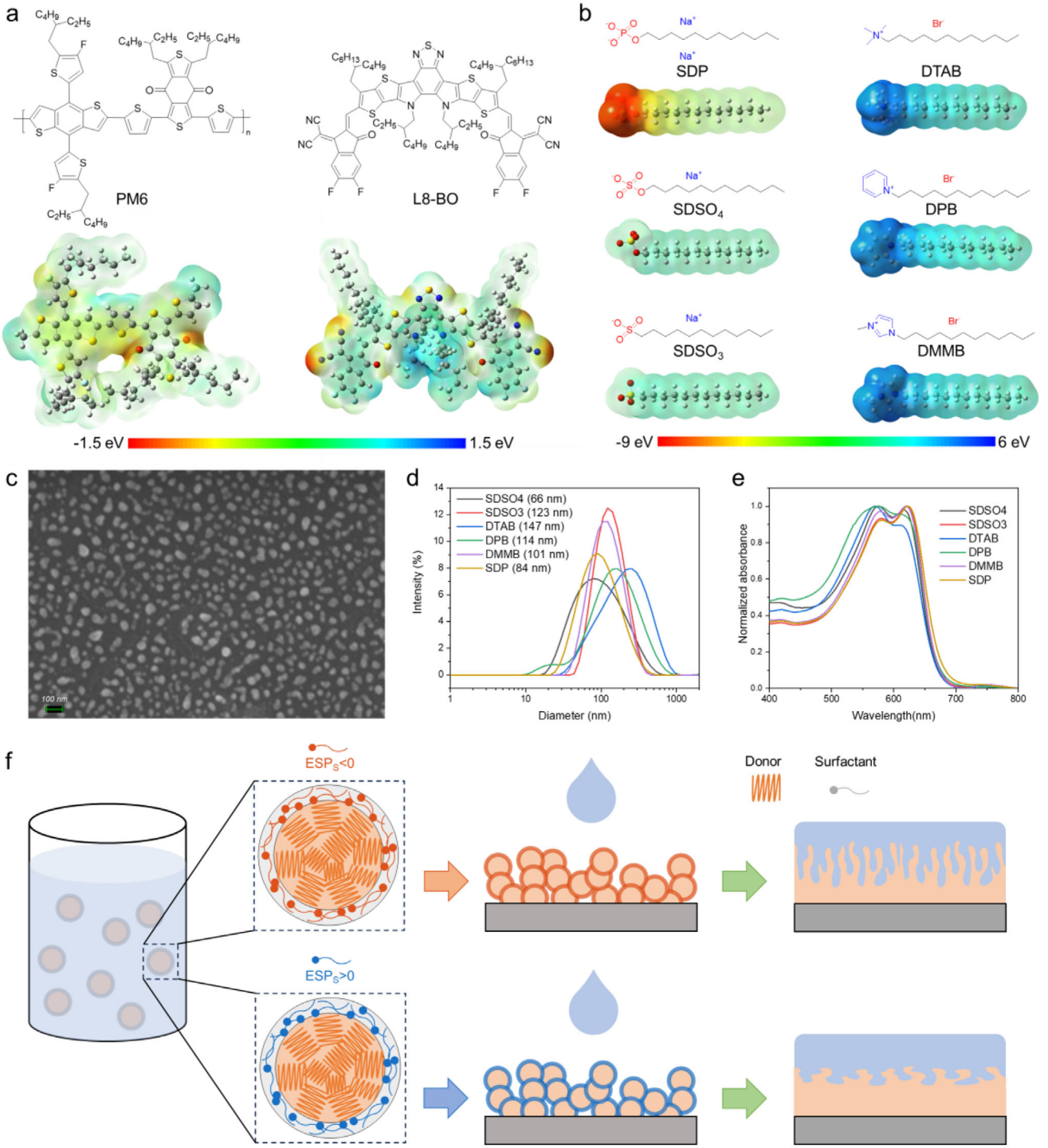

Figure 1. a) Chemical structure and ESP of PM6, L8-BO and different surfactants; b) SEM of dried PM6 NPs with SDP as surfactant; d) Particle size distribution and e) UV–vis absorption spectra of PM6 NPs dispersion with various surfactants; f) Schematic diagram of mn-LBL processing of active layer with donor NPs with different surfactant ESP values.

LBL methods, where insufficient D/A interaction often limits morphological control.

The interfacial characteristics of the mesostructured nanoparticle (mn) layer critically govern both the subsequent acceptor deposition and the resulting vertical phase morphology of the active layer. Before the film deposition, a centrifugal washing process was used to minimize the content of surfactant in those NP systems (see Supporting Information).[25] As shown in Figure S3 (Supporting Information), the retention of all those 6 surfactants was found to be less than 5% after repeated washing

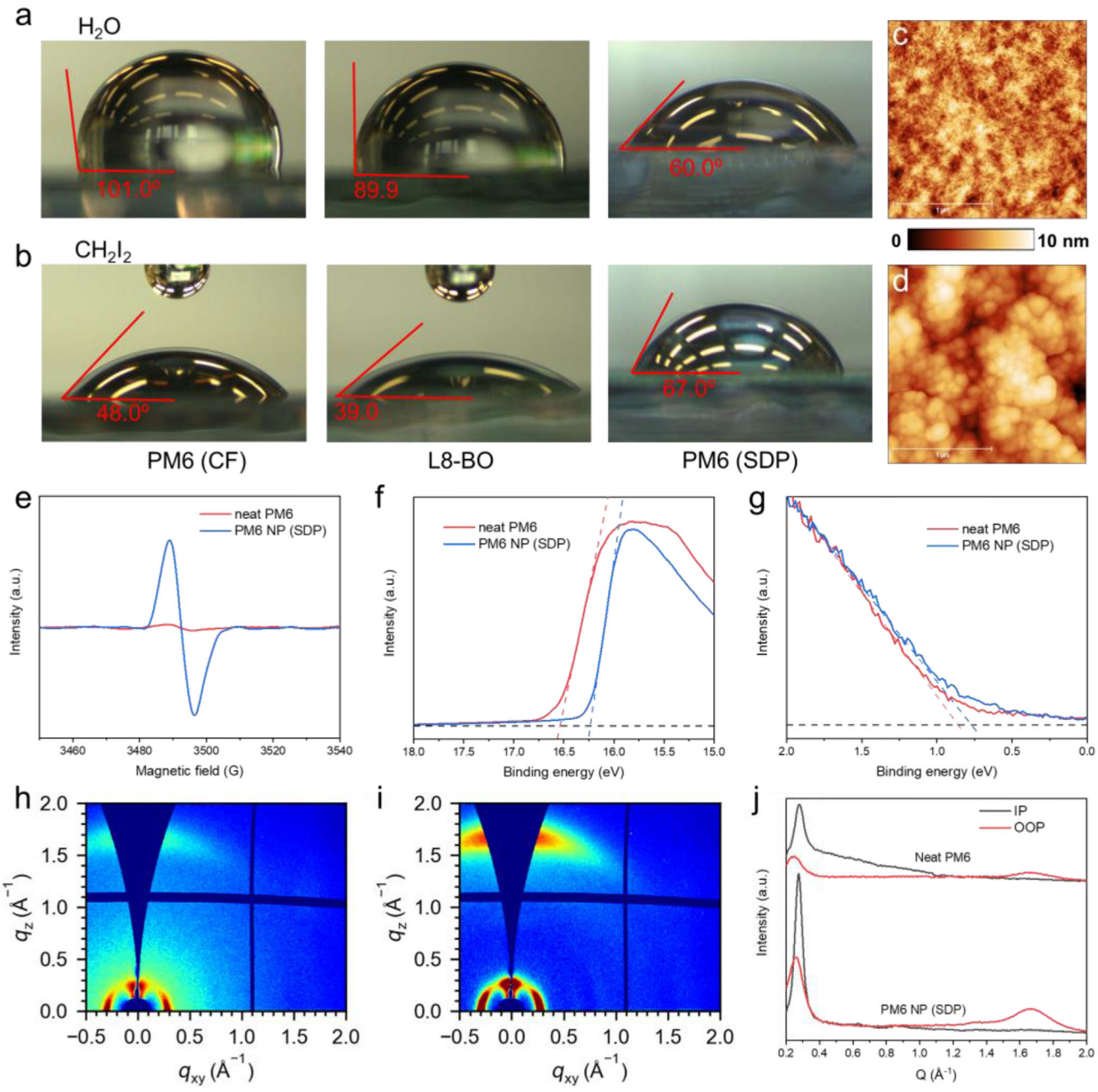

Figure 2. Contact angle of a) water and b) CH_2I_2 on top of toluene-processed neat PM6, L8-BO, and PM6 NP films. AFM images of c) neat PM6 and d) PM6 NP films. e) EPR spectra as well as UPS spectra at the range of f) the secondary electron cutoff edge (E_{SE}) and g) the valence band energy (E_{VB}) of neat PM6 and PM6 NP films. 2D GIWAXS patterns of h) neat PM6 and i) PM6 NP films, as well as j) their corresponding in-plane and out-of-plane line-cuts.

steps. Spin-coating of these purified NP dispersions yielded mesoporous architectures featuring well-defined spherical motifs and interconnected cavities, as verified by scanning electron microscopy (SEM) and atomic force microscopy (AFM) characterization (**Figure** 2d; Figure S4, Supporting Information). This unique morphology promotes enhanced acceptor interdiffusion during the layer-by-layer deposition process. Contact angle measurements revealed significant surface energy (γ) variations between mn-films and conventional bulk heterojunction (BHJ) systems, with SDP-modified PM6 films exhibiting $\gamma = 44.0$ mN m^{-1} compared to 32.4 mN m^{-1} for BC films (Figure 2a,b; Table S3, Supporting Information). This 36% increase in surface energy is attributed to residual hydrophilic surfactant moieties that survive the purification process. Quantitative analysis of intermolecular interactions through Flory-Huggins parameters ($\chi_{PM6:L8-BO} = \left(\sqrt{\gamma_{PM6}} - \sqrt{\gamma_{L8-BO}}\right)^2$) demonstrated remarkable compatibility enhancement, with SDP-based mn-films achieving $\chi = 0.053$ versus 0.506 for neat PM6 - representing an order-of-magnitude

improvement in donor-acceptor miscibility through nanoparticle engineering.[32]

Beyond facilitating donor-acceptor (D/A) intermolecular interactions, ionic surfactants were found to concurrently induce p-type doping in the donor semiconductor matrix.[33] This doping mechanism originates from redox reactions between surfactant molecules and the organic semiconductor, wherein charge transfer generates additional holes in the highest occupied molecular orbital (HOMO).[34] Comprehensive characterization using electron paramagnetic resonance (EPR) spectroscopy revealed characteristic split peaks at 348.8 and 349.6 mT (Figure 2e; Figure S6, Supporting Information), unambiguously confirming the formation of radical species in PM6 nanoparticle (NP) films (Figure 2e; Figure S6, Supporting Information).[35] Ultraviolet photoelectron spectroscopy (UPS) analysis provided quantitative evidence of doping effects through two key observations: a) The Fermi level to HOMO energy gap (E_F-E_{HOMO}) narrowed from −0.86 eV in pristine PM6 to −0.77 eV in SDP-modified NPs (Figure 2f,g), calculated using:

$$\mathrm{EHOMO} = h\nu - (\mathrm{ESE} - \mathrm{EVB}) \quad (1)$$

$$\mathrm{WF} = h\nu - \mathrm{ESE} \quad (2)$$

where E_{SE} represents the secondary electron cutoff edge (16.54 eV vs 16.25 eV for neat and NP films, respectively), and E_{VB} denotes the valence band maximum (0.86 eV vs 0.77 eV); b) Consistent p-doping behavior was observed across all anionic surfactants (SDSO4, SDSO3), as evidenced by similar Fermi level shifts (Figure S7 and Table S4, Supporting Information). These findings collectively demonstrate that anionic surfactant incorporation during mn-LBL processing serves a dual purpose: i) enhancing interfacial D/A interactions through electrostatic effects, and ii) improving charge transport properties via controlled p-doping of the donor phase.

The molecular organization and crystalline structure of PM6 mn-films incorporating various surfactants were systematically investigated using grazing-incidence wide-angle X-ray scattering (GIWAXS). As depicted in Figure 2h–j, both neat PM6 and PM6 NP (SDP) films present a distinct (010) π–π stacking peak at qz ≈1.65 Å^{-1} in the out-of-plane (OOP) direction and a well-defined lamellar (100) diffraction peak at q_{xy} ≈0.275 Å^{-1} in the in-plane (IP) direction, indicative of its preferential face-on orientation with respect to the substrate.[36] Notably, surfactant-incorporated NP films displayed substantial enhancement in structural order parameters. The NP films with anionic SDP or cationic DMMB both demonstrate significantly enlarged coherence lengths (CCL) for the (010) (OOP) and (100) (IP) peaks, respectively, signifying enhanced face-on orientation of PM6 molecules (Figure S8 and Table S5, Supporting Information). This pronounced improvement in crystalline ordering establishes a favorable charge transport pathway orthogonal to the substrate plane - a critical factor for enhancing device performance in OSCs.

We fabricated conventional architecture organic solar cells (OSCs) employing the mn-LBL processing strategy. The device fabrication process involved sequential deposition of aqueous PM6 NP inks on 2PACz-modified substrates, followed by acceptor (L8-BO) solutions in various organic solvents. Three solvent systems were evaluated for acceptor processing: chloroform (CF), o-xylene (o-XY), and toluene (Tol). Active layers with thicknesses of 100, 200, 300, and 400 nm were fabricated by varying the concentration of the NP inks and acceptor solutions (see Supporting Information). As depicted in **Figure 3**a and **Table 1**, current density-voltage (J-V) characterization revealed outstanding performance metrics. As shown in Figure S9 (Supporting Information), the mn-LBL (SDP) OSCs processed by Tol produced an optimized PCE of 19.97% at a 100 nm active layer thickness (certified value of 19.46%, Figures S10–S14, Supporting Information), with an open-circuit voltage (V_{OC}) of 0.90 V, a short-circuit current (J_{SC}) of 27.70 mA cm^2, and a fill factor (FF) of 80.4%. Remarkably, these devices maintained outstanding performance at increased active layer thicknesses, delivering a PCE of 18.87% (certified 18.32%, Figures S15–S19, Supporting Information) at 300 nm with a V_{OC} of 0.89 V, J_{SC} of 27.74 mA cm^2, and an FF of 76.20% (Figure 3a), representing among the highest reported certified efficiencies for thick-film organic solar cells (Table S6, Supporting Information). The BC device exhibits a sharp PCE drop at high thickness. Compared to LBL counterparts, random phase separation in thickened BC films generates isolated D/A domains and interfacial defects, which significantly enhance bimolecular recombination and severely compromise charge extraction efficiency in OSCs. The universality of this approach was further demonstrated through successful implementation with alternative processing solvents (CF and o-XY), all of which showed comparable performance enhancements (Figures S20, S21, Table S7 and S8, Supporting Information). Furthermore, the mn-LBL OSCs with different surfactants were also fabricated. As shown in Figure S22 and Table S9 (Supporting Information), comparative analysis of different surfactant systems revealed that anionic variants (SDSO4, SDSO3) consistently outperformed their cationic counterparts, yielding devices with PCEs exceeding 19% and demonstrating superior thickness tolerance. This performance superiority is attributed to the enhanced electrostatic potential difference between donor and acceptor materials induced by anionic surfactants. In addition, LBL control devices processed using donor solutions containing an anionic surfactant exhibit enhanced Voc values rather than improvements in Jsc or FF (Figure S23 and Table S10, Supporting Information). This suggests that while p-doping primarily contributes to the Voc enhancement, electrostatic interactions dominate the gains in Jsc and FF, ultimately leading to the superior performance observed in mn-LBL devices. Furthermore, external quantum efficiency (EQE) measurements showed excellent consistency with J-V characteristics (<5% mismatch in J_{SC} values), while revealing reduced EQE responses between 400–600 nm for conventional BC and LBL control devices at 300 nm thickness, indicative of compromised photon harvesting in these architectures (Figure 3b).

Charge transport dynamics and recombination behavior were systematically investigated to understand the superior performance of mn-LBL devices. The voltage-light intensity dependence analysis revealed distinct charge trapping characteristics, where the slope values of 1.37 kT q^{-1} for c-LBL and 1.10 kT q^{-1} for mn-LBL (SDP) devices (at 300 nm thickness) indicate significantly suppressed trap-assisted recombination in the surfactant-engineered system (Figure 3c), where k is the Boltzmann constant, T is Kelvin temperature, and q is the elementary charge.[37] In addition, devices incorporating SDP surfactant demonstrated

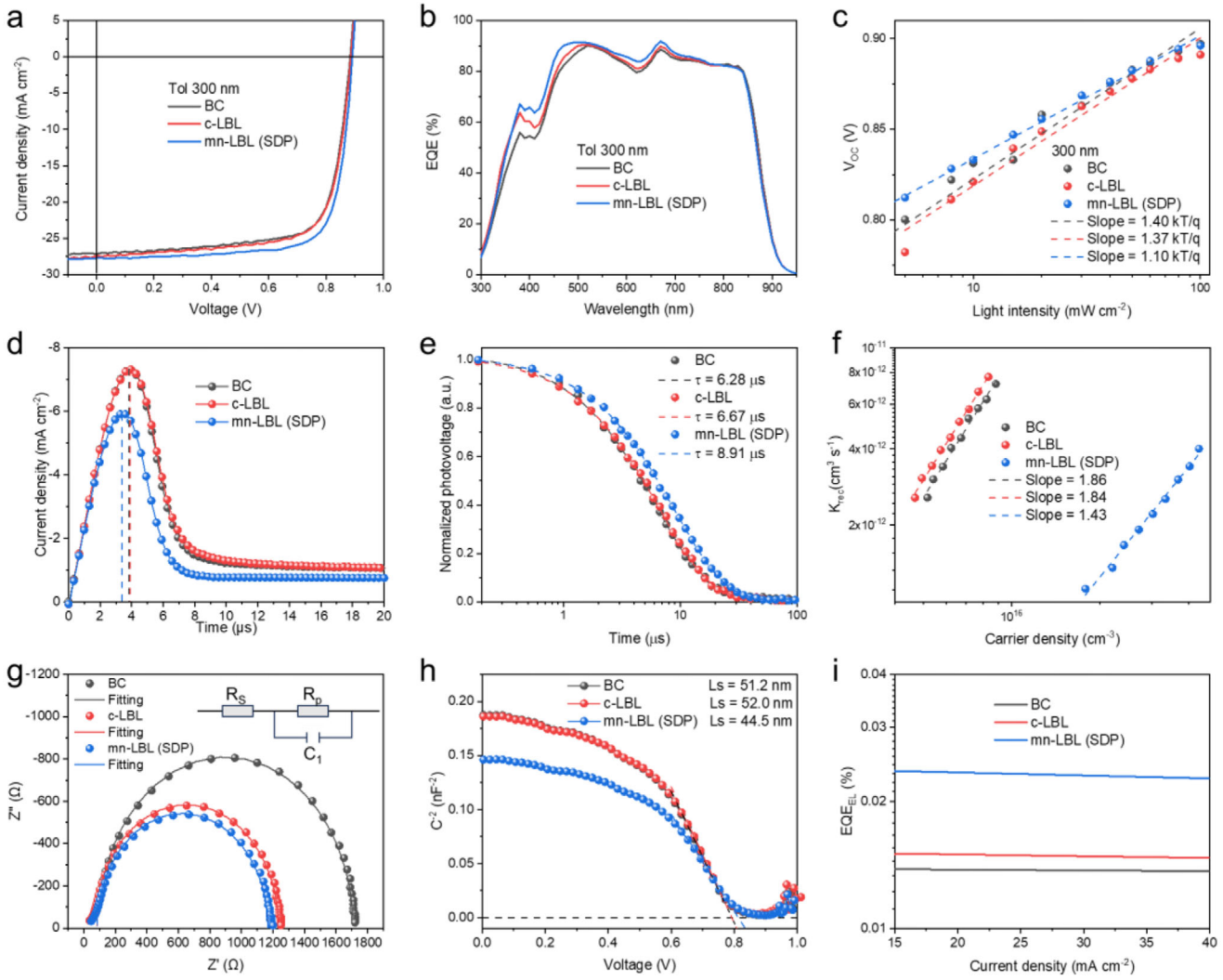

Figure 3. a) J-V characteristics, b) EQE spectra, c) light intensity as a function of Voc, d) photo-CELIV curves, e) TPV curves, f) bimolecular recombination rate constant (K_{rec}) as a function of carrier density, g) Nyquist plots, h) Mott-Schottky plots, and i) EQE_{EL}s of PM6:L8-BO-based solar cells with an active layer thickness of 300 nm prepared by various processing strategies.

Table 1. Summary of photovoltaic parameters of toluene processed PM6:L8-BO solar cells with different thicknesses and processing methods.

Thickness [nm]	Processing method	V_{OC} [V]	J_{SC} [mA cm^{-2}]	J_{SC}[a)] [mA cm^{-2}]	FF [%]	PCE[b)] [%]
100	BC	0.896	26.95	25.89	79.40	19.18 (18.95 ± 0.23)
±	c-LBL	0.894	27.055	26.09	78.42	18.97 (18.59 ± 0.38)
10	mn-LBL[c)]	0.897	27.695	26.70	80.41	19.97 (19.58 ± 0.38)
200	BC	0.883	27.47	26.47	76.49	18.56 (18.38 ± 0.18)
±	c-LBL	0.881	27.35	26.58	76.16	18.35 (18.15 ± 0.20)
20	mn-LBL[c)]	0.882	27.78	26.81	77.85	19.07 (18.85 ± 0.22)
300 ± 20	BC	0.883	26.79	25.96	73.49	17.38 (17.09 ± 0.29)
	c-LBL	0.885	27.54	26.55	72.30	17.62 (17.38 ± 0.24)
	mn-LBL[c)]	0.889	27.74	27.07	76.20	18.87 (18.54 ± 0.31)
400 ± 30	BC	0.867	27.03	25.95	63.707	14.93 (14.61 ± 0.32)
	c-LBL	0.876	27.40	26.79	66.60	15.99 (15.83 ± 0.21)
	mn-LBL[c)]	0.879	27.82	27.11	70.82	17.30 (17.00 ± 0.30)

[a)] Calculated from EQE; [b)] Average values with standard deviation were obtained from 20 devices; [c)] Processed from PM6 NPs with SDP as surfactant.

superior performance to those with SDSO3 or DMMB (Figure S23, Supporting Information), attributed to the dual anionic groups in SDP more effectively passivating trap states under open-circuit conditions. Moreover, photo-induced charge carrier extraction by linearly increasing voltage (photo-CELIV) measurements quantified the enhanced charge transport properties, revealing a 30% improvement in average carrier mobility (1.12×10^{-4} cm^2 $V^{-1}s^{-1}$) for mn-LBL (SDP) devices compared to conventional LBL controls (8.55×10^{-5} cm^2 $V^{-1}s^{-1}$) (Figure 3d). Transient photovoltage (TPV) and transient photocurrent (TPC) measurements further corroborate the enhanced charge extraction efficiency and extended carrier lifetime in OSCs. The mn-LBL (SDP) device exhibits a prolonged charge carrier lifetime (τ = 8.91 µs), exceeding the control device value (6.67 µs) (Figure 3e; Figure S25, Supporting Information). These synergistic improvements in charge mobility, carrier lifetime, and extraction kinetics collectively underpin the elevated Jsc and FF values observed in surfactant-optimized devices.

Detailed recombination analysis through TPV & charge exaction (CE) measurements provided additional insights into the charge dynamics.[25,38] The bimolecular recombination coefficient Krec = $1/(\lambda+1)n\tau$, where λ is the recombination order and n is the carrier density, was calculated from the TPV & CE results (Figure 3f).[38] The two control systems exhibit a much higher order of Krec dependency (slope = 1.86 for BC and 1.84 for c-LBL, respectively) compared to that of mn-LBL (SDP) device (slope = 1.43). Significantly suppressed charge carrier recombination in mn-LBL device with SDP indicates a superior charge dynamic in comparison with 300 nm-thick devices with other surfactants (Figure S26, Supporting Information). Electrochemical impedance spectroscopy (EIS) measurements exhibit a reduction of series resistance (Rs) by applying mn-LBL strategy for device fabrication, suggesting a promoted charge transport (Figure S27 and Table S11, Supporting Information).[39] The comprehensive charge dynamics characterization consistently demonstrates that the SDP-modified mn-LBL approach effectively mitigates loss mechanisms while enhancing charge transport throughout the active layer.

Charge transport mechanisms in OSCs are governed by two distinct processes: drift transport induced by internal electric fields and diffusion driven by charge density gradients. As illustrated in Figure S28 (Supporting Information), these processes operate in spatially distinct regions of the device architecture.[40] The space-charge region, localized near the cathode interface due to work function differences with PNDIT-F3N, primarily facilitates drift-dominated transport. In contrast, diffusion mechanisms prevail throughout the remaining flat-band region of the active layer.[41] Quantitative analysis of space-charge region (L_S) characteristics was performed using Mott-Schottky formalism:[35]

$$\frac{1}{C^2} = \frac{2}{q\varepsilon_0\varepsilon_r A^2 N_A}(V_{bi} - V) \tag{3}$$

$$L_S = \frac{\varepsilon_0\varepsilon_\gamma}{C} = \sqrt{\frac{2\varepsilon_0\varepsilon_r}{qA^2N_A}\left(V_{bi} - V\right)} \tag{4}$$

where N_A is the density of space-charge (or defects), V_{bi} is the built-in voltage, A is the device area, q is the elementary charge, ε_0 is the permittivity of vacuum, and ε_r is the relative permittivity. The flat band region width (L_N) was determined from the active layer thickness (d) as $L_N = d - L_S$. Comparative analysis (Figure 3h) shows the L_S decreased significantly from 52 nm in control devices to 45 nm in mn-LBL (SDP) systems for 300 nm-thick active layers. Consequently, L_N increased from 249 to 255 nm. This expanded flat band region now accounts for > 80% of the active layer thickness – a regime where relatively rapid bimolecular recombination typically occurs, as charge carriers primarily exit via diffusion.[42] Within the space-charge region, balanced charge transport prevents screening of the internal electric field by accumulated (trapped) charges. The SDP-induced p-doping is thus expected to modify critical charge transport lengths: the diffusion length (L_{dif}) and drift length (L_{dr}). These were calculated using: $L_{dif} = (D\tau)^{0.5}$ and $L_{dr} = E\mu\tau$, with the diffusion coefficient (D) derived from the Einstein relation $D/\mu = k_BT/q$. Here, τ represents carrier lifetime (from TPV), μ denotes mobility (from photo-CELIV), k_B is Boltzmann constant, T is room temperature, q is the elementary charge, and E is electric field intensity. Calculations reveal L_{dif} increases from increased from 38.39 nm (c-LBL) to 50.79 nm (mn-LBL). The enhancement in L_{dr} is more substantial, rising from 456 to 798 nm. These enhanced transport lengths directly originate from the p-doping effect in the mn-LBL (SDP) architecture, which effectively mitigates the increased bimolecular recombination risk associated with the elongated L_N.

Furthermore, the energy loss mechanisms in mn-LBL processed OSCs were quantitatively analyzed through complementary FTPS and EL spectroscopy measurements (Figure S30, Supporting Information).[43] Generally, the total energy loss (E_{loss}) can be systematically deconvoluted into three distinct components: first, the inherent radiative recombination loss (ΔE_1) arises from the thermodynamic limit defined by the difference between the material bandgap (E_g) and the maximum theoretically achievable voltage according to Shockley-Queisser formalism. This fundamental loss component represents an unavoidable consequence of blackbody radiation in photovoltaic devices. Second, additional radiative losses (ΔE_2) occur due to deviations from ideal absorption characteristics, including band tail states and sub-bandgap charge transfer absorption, which stem from structural disorder in the active layer; third, the magnitude of non-radiative recombination loss (ΔE_3) is quantitatively determined through the relationship $-k_BTln(EQE_{EL})$, where k_B is the Boltzmann constant and T is temperature. As shown in Table S12 (Supporting Information), the E_g of active layers with various processing strategies are measured the same as 1.446 eV. Meanwhile, the incorporation of surfactant did not cause any additional absorption of sub-gap states in FTPS-EQE measurement (Figure S30, Supporting Information), which indicates the radiative recombination loss (ΔE_1) of optimized mn-LBL devices very close to the control device (≈0.07 eV). However, the non-radiative energy loss (ΔE_3) decreases significantly from 0.228 to 0.215 eV after applying mn-LBL (SDP) strategy, corresponding to EQE_{EL} values of 1.38×10^{-4} and 2.37×10^{-4}, respectively (Figure 3i). As a result, the E_{loss} of devices from BC, c-LBL, and mn-LBL (SDP) processing strategies are calculated to be 0.570, 0.566, and 0.546 eV, respectively. Therefore, the reduced E_{loss} originates from two synergistic effects: i) the p-doping behavior induced by anionic surfactants that improves charge collection, and ii) the optimized vertical morphology that reduces trap-assisted

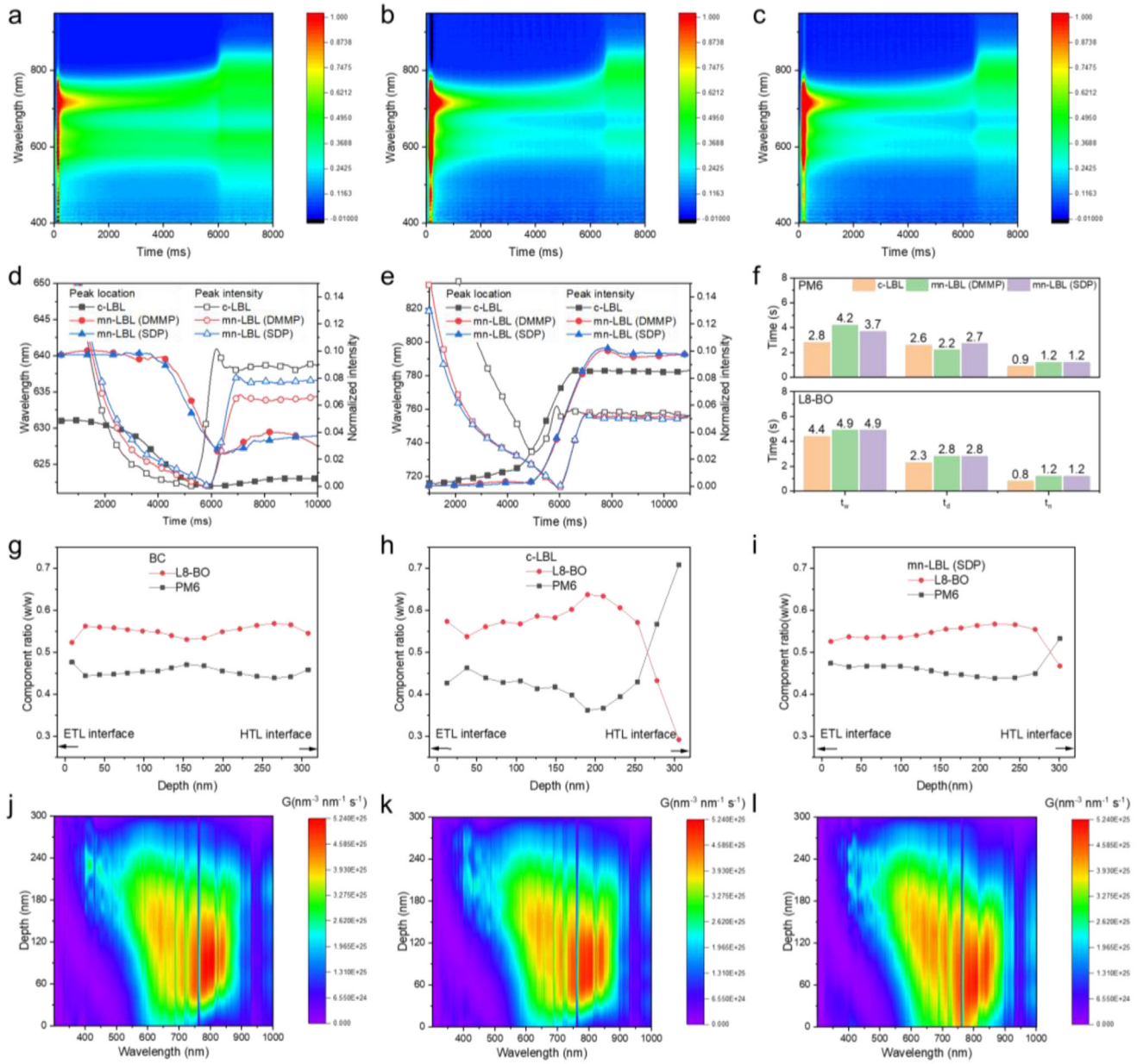

Figure 4. Time-dependent contour maps of UV–vis absorption spectra for a) conventional LBL film, b) mn-LBL film with surfactant DMMB, and c) mn-LBL film with surfactant SDP processed by toluene. Time evolution of peak location and intensity of d) PM6 and e) BTP-eC9. f) Histogram of washing time (t_w), drying time (t_d), and nucleation time (t_n) for those films during LBL process. g–i) Composition ratio in the vertical direction and j–l) exciton generation contours of the (g,j) BC, (h,k) conventional LBL, and (I,l) mn-LBL (SDP) active layer films.

recombination pathways.[44–46] These modifications collectively contribute to the superior device performance while maintaining the fundamental thermodynamic limits of the material system.

To elucidate the structure-property relationships governing device performance in mn-LBL OSCs, we conducted in situ UV–vis absorption monitoring of the film formation dynamics. Real-time UV–vis absorption spectroscopy revealed distinct morphological evolution pathways during layer deposition, as evidenced by temporal changes in spectral features for conventional LBL (c-LBL), DMMB-modified, and SDP-optimized systems (**Figure** 4a–c). Significant shifts in donor and acceptor peak positions and intensities, observed during spin-coating-based LBL assembly, indicated altered molecular aggregation in all samples. The spectral evolution exhibited three characteristic kinetic phases: i) an initial solvent washing stage marked by rapid spectral shifts, ii) an intermediate drying period showing gradual peak intensity changes, and iii) a final nucleation phase demonstrating stabilization of absorption characteristics.[22] As depicted in Figure 4f, Comparative analysis of these temporal profiles revealed that mesoporous donor layers extended the washing phase duration (t_w) from 6.3 s (c-LBL) to 7.6 s (SDP-modified mn-LBL), indicating enhanced acceptor penetration through the nanostructured

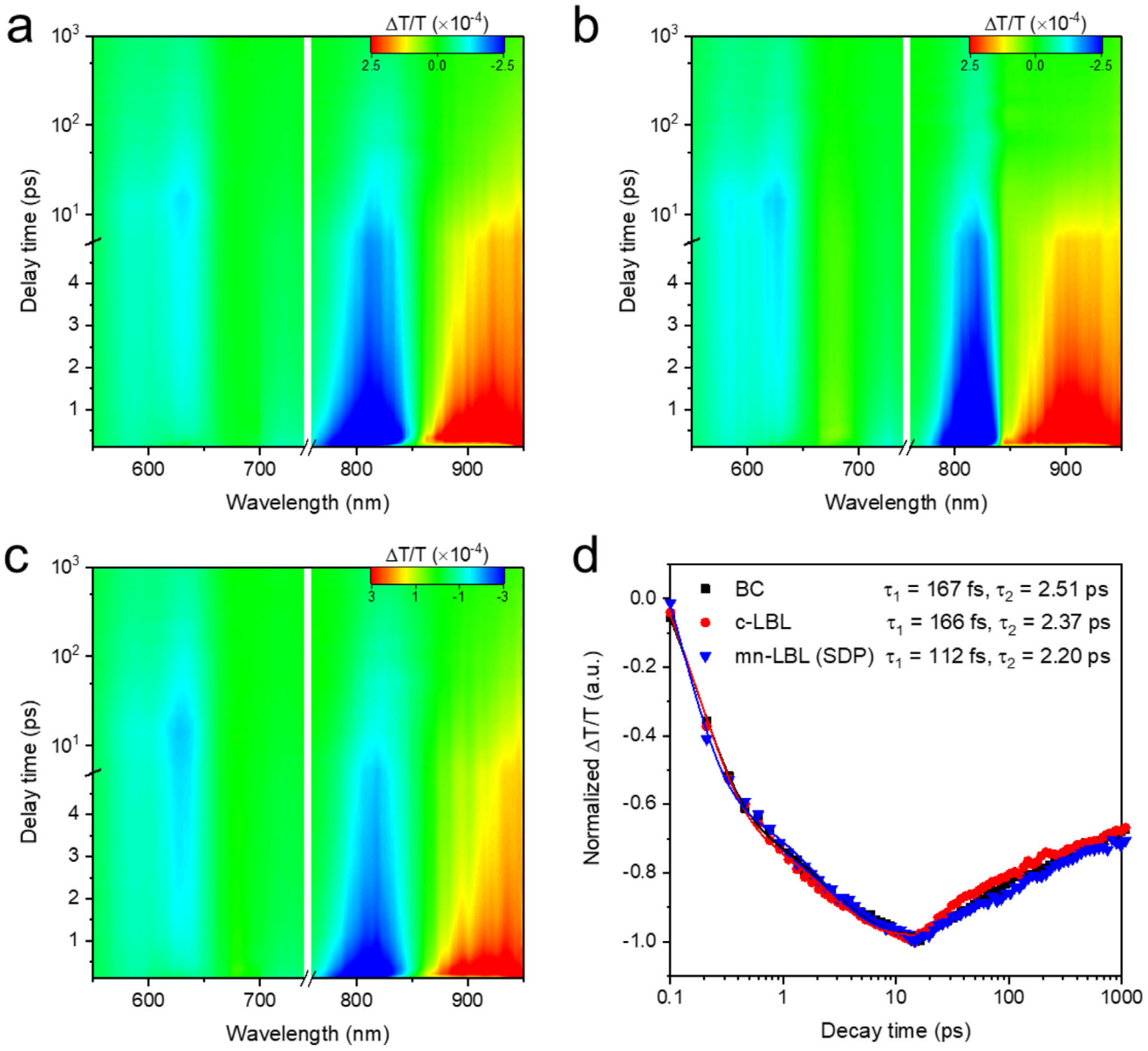

Figure 5. 2D fs-TA contour at different time delays of PM6:L8-BO films processed by a) BC, b) conventional LBL and c) mn-LBL (SDP) techniques as well as their corresponding Fs-TA decay dynamics probed at 625 nm.

underlayer. Additionally, SDP-containing films displayed a prolongation of the drying phase (t_d) relative to control samples, consistent with surfactant-mediated modulation of intermolecular interactions at the donor-acceptor interface. The subsequent nucleation stage (t_n) in optimized systems manifested both extended transition times and pronounced bathochromic shifts, spectroscopic signatures indicative of improved molecular ordering and crystallinity. These observations collectively demonstrate how surfactant engineering influences the hierarchical assembly process, ultimately yielding morphologies with enhanced charge transport characteristics.

To investigate the vertical phase distribution resulting from surfactant-enhanced electrostatic interactions in the mn-LBL process, we employed film-depth-dependent light absorption spectroscopy (FLAS) to characterize the 300 nm-thick active layers. As shown in Figure 4g, BC films showed homogeneous vertical distribution of PM6 and L8-BO, both LBL approaches exhibited donor enrichment near the substrate interface - a configuration known to promote efficient hole extraction at the anode.[17] However, a massive accumulation of PM6 at the bottom was observed in c-LBL film, indicating limited donor-acceptor interdiffusion. In contrast, a gentle rise of PM6 ratio with a pronounced region of excitons near the bottom was observed in the mn-LBL films (Figure 4i; Figure S31, Supporting Information). These findings indicate that the mn-LBL strategy with strong intermolecular interaction provides sufficient D/A interpenetration to maintain efficient charge generation throughout the thick (300 nm) active layer. In addition, appropriate donor enrichment at the

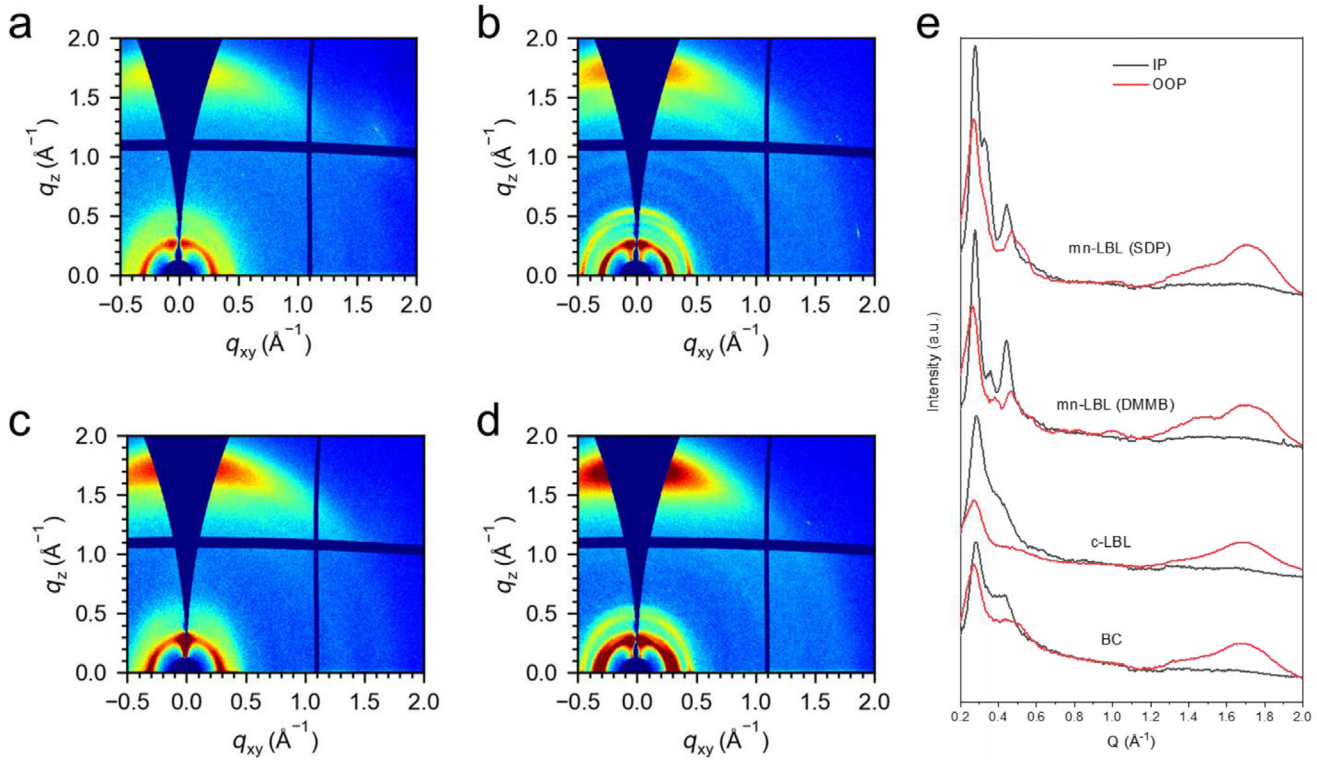

Figure 6. 2D GIWAXS patterns of PM6:L8-BO films processed by a) BC, b) conventional LBL, c) mn-LBL (DMMB), and d) mn-LBL (SDP) techniques, as well as e) their corresponding in-plane and out-of-plane line-cuts.

anode interface to facilitate charge collection while minimizing recombination losses. These morphological improvements correlate directly with enhanced device performance metrics, including reduced bimolecular recombination coefficients (Krec) and improved charge extraction kinetics.

Ultrafast charge transfer dynamics in mn-LBL processed films were elucidated through femtosecond transient absorption spectroscopy (fs-TA) with careful control of experimental parameters. Using a low pump fluence (2 μJ cm^{-2}) at 750 nm excitation wavelength, we selectively probed the hole transfer dynamics from photoexcited L8-BO to the PM6 donor while minimizing exciton-exciton annihilation effects.[47] As shown in **Figure** 5a–c, spectral analysis revealed characteristic excited-state features, including ground-state bleaching (GSB) at 820 nm and excited-state absorption (ESA) at 925 nm, with the hole transfer kinetics monitored through the evolution of PM6's GSB signal at 625 nm. As shown in Figure 5d, The ≈15 ps rise dynamics of the PM6 GSB signal signify hole transfer from acceptor to donor. For the mn-LBL (SDP) film, biexponential analysis of this signal revealed a fast component (τ_1 = 112 fs) corresponding to ultrafast interfacial exciton dissociation, and a slower component (τ_2 = 2.20 ps) associated with exciton diffusion in the acceptor prior to reaching the interface.[48] Comparative studies demonstrated significant kinetic advantages in SDP-modified films, with interfacial charge transfer rates 50% faster than BC (τ_1 = 248 fs) and C-LBL (τ_1 = 284 fs) counterparts. Furthermore, the surfactant-dependent dynamics were further evidenced by DMMB-containing films showing slightly faster τ_1 (105 fs) but slower τ_2 (2.61 ps) components (Figure S32, Supporting Information), highlighting the critical role of specific surfactant chemistry in governing exciton behavior. These findings directly link the electrostatic interactions inherent to the mn-LBL approach with improved donor-acceptor contact and accelerated hole transfer from L8-BO to PM6, further verifying the contribution that can make to improving the J_{SC} and FF in OSCs.

Building upon the established correlation between electrostatic interactions and morphological control, we conducted quantitative crystallographic analysis to further understand the performance enhancement in mn-LBL devices. Grazing-incidence wide-angle X-ray scattering (GIWAXS) measurements revealed that all LBL-processed films maintained preferential face-on molecular orientation, as evidenced by a pronounced π–π stacking peak (010) at q_z = 1.69 ± 0.01 Å^{-1} in the OOP direction and distinct lamellar stacking (100) at q_{xy} = 0.28 Å^{-1} in the IP direction (**Figure 6**). As detailed in Table S5 (Supporting Information), SDP-modified films exhibited an increase in CCL for both crystallographic directions compared to conventional LBL films, demonstrating that surfactant-induced electrostatic interactions promote long-range molecular ordering while preserving the desired orientation for vertical charge transport.[49] These structural advantages directly correlate with the enhanced charge carrier mobility observed in photo-CELIV measurements.

The versatility of the SDP-based mn-LBL approach was further demonstrated through successful implementation with multiple acceptor systems. When applied to binary (PM6:BTP-eC9) and ternary (PM6:L8-BO:BTP-eC9) blends processed with environmentally benign solvents (water for donor and toluene for acceptor), the strategy consistently delivered performance

improvements across all systems (Table S13 and Figure S33, Supporting Information). Most remarkably, the mn-LBL (SDP) PM6:L8-BO:BTP-eC9 devices demonstrated an impressive champion PCE of 20.30% (certified value of 19.86%, Figures S34–S39, Supporting Information), with a V_{OC} of 0.90 V, J_{SC} of 27.98 mA cm^{-2}, and FF of 80.86%, which outperformed the c-LBL solar cells with a PCE of 18.94%. This achievement is particularly significant as it establishes new performance benchmarks for halogen-free processed OSCs, while simultaneously demonstrating the feasibility of aqueous processing for the donor layer deposition. The universal applicability of this SDP-modified mn-LBL approach across different material systems highlights its potential as a general strategy for high-performance OSCs.

3. Conclusion

This work demonstrates a groundbreaking aqueous processing strategy that successfully overcomes the thickness limitations of high-efficiency organic solar cells through innovative layer-by-layer (LBL) fabrication. By engineering water-based nanoparticle donor inks incorporating strategically designed surfactants, we achieved exceptional control over donor-acceptor interdiffusion and vertical phase distribution. DFT calculations revealed that anionic surfactants, particularly the doubly charged SDP molecule, create optimal electrostatic potential gradients for enhanced donor-acceptor interactions. EPR and UPS results confirmed that anionic surfactants simultaneously enable p-doping of the donor matrix and improved interfacial energetics. Morphology investigation techniques, including in situ UV–vis absorption, FLAS, and GIWAXS, revealed the alleviation of vertical phase separation and formation of high crystalline when mn-LBL processing active layer with high thickness. The optimized morphology led to efficient carrier separation and transport in thickened OSCs, being detected by TA and photo-CELIV. A binary system processed by water-borne PM6 with surfactant SDP and a non-halogenated toluene solution of L8-BO delivered a PCE close to 20%. The mn-LBL (SDP) OSCs showed one of the best thickness tolerances and achieved PCEs of 18.9% and 17.3% with thicknesses of 300 and 400 nm, respectively. Moreover, employing mn-LBL (SDP) into the ternary PM6:L8-BO:BTP-eC9 system gave an outstanding PCE of 20.3% (19.9% certified). The demonstrated performance metrics, achieved through fundamental understanding of electrostatic and doping effects, set new benchmarks for environmentally friendly OSC fabrication while providing a versatile platform for future device optimization.

Supporting Information

Supporting Information is available from the Wiley Online Library or from the author.

Acknowledgements

C.X., X.W., and H.C. contributed equally to this work. The authors are grateful for the support from the National Natural Science Foundation of China (no. 12274303 and no. 52333006). H.L. thanks for the support from the Natural Science Foundation of Top Talent of SZTU (grant no. GDRC202307). Z.T. thanks for the support from Guangdong Higher Education Letter [2024] No. 30. S.L. would like to thank the support from the Education Department of Guangdong Province (No. 2024ZDJS064). B.H. and P.H. appreciate the support from Shenzhen Key Laboratory of Applied Technologies of Super-Diamond and Functional Crystals (ZDSYS20230626091303007). L.H. thanks for the Central University Basic Research Business Funding Project (2023SCU12021). C.X. thanks for the support from Development of new perovskite optoelectronics (contract No. HT20231107001) and Development of printable organic optoelectronics (contract No. HT20241118001). T.X. thanks for the support from Research and development of new multifunctional thin-film optoelectronic devices (HX-0742) and Shenzhen overseas high-level talents Peacock plan scientific research project (RC2024-004). This work was carried out with the support of the Shanghai Synchrotron Radiation Facility (SSRF), beamline BL02U2. The authors thank SSRF BL02U2 for 2D GIWAXS measurements.

Conflict of Interest

The authors declare no conflict of interest.

Data Availability Statement

The data that support the findings of this study are available from the corresponding author upon reasonable request.

Keywords

layer-by-layer, organic semiconductor nanoparticles, organic solar cells, surfactant engineering, water-processing

Received: May 9, 2025
Revised: July 10, 2025
Published online:

[1] H. Chen, Y. Huang, R. Zhang, H. Mou, J. Ding, J. Zhou, Z. Wang, H. Li, W. Chen, J. Zhu, Q. Cheng, H. Gu, X. Wu, T. Zhang, Y. Wang, H. Zhu, Z. Xie, F. Gao, Y. Li, Y. Li, *Nat. Mater.* **2025**, *24*, 444.
[2] W. Zou, Y. Sun, L. Sun, X. Wang, C. Gao, D. Jiang, J. Yu, G. Zhang, H. Yin, R. Yang, H. Zhu, H. Chen, K. Gao, *Adv. Mater.* **2025**, *37*, 2413125.
[3] J. Deng, W. Li, R. Zeng, J. Song, S. Tan, L. Kan, Z. Qin, *Adv. Mater.* **2025**, *37*, 2501243.
[4] L. Guo, J. Song, J. Deng, J. Qiao, J. Zhang, C. Li, S. Yuan, B. Han, M. H. Jee, Z. Ge, C. Zhang, G. Lu, X. Hao, *Adv. Mater.* **2025**, *37*, 2504396.
[5] Y. Wang, C. Gao, W. Lei, T. Yang, Z. Liang, K. Sun, C. Zhao, L. Chen, L. Zhu, H. Zeng, X. Sun, B. He, H. Hu, Z. Tang, M. Qiu, S. Li, P. Han, G. Zhang, *Nano-Micro Lett.* **2025**, *17*, 206.
[6] S. Guan, Y. Li, C. Xu, N. Yin, C. Xu, C. Wang, M. Wang, Y. Xu, Q. Chen, D. Wang, L. Zuo, H. Chen, *Adv. Mater.* **2024**, *36*, 2400342.
[7] H. Zhang, Y. Liu, G. Ran, H. Li, W. Zhang, P. Cheng, Z. Bo, *Adv. Mater.* **2024**, *36*, 2400521.
[8] L. Zhan, S. Yin, Y. Li, S. Li, T. Chen, R. Sun, J. Min, G. Zhou, H. Zhu, Y. Chen, J. Fang, C. Q. Ma, X. Xia, X. Lu, H. Qiu, W. Fu, H. Chen, *Adv. Mater.* **2022**, *34*, 2206269.
[9] J. Luke, L. Corrêa, J. Rodrigues, J. Martins, M. Daboczi, D. Bagnis, J. S. Kim, *Adv. Energy Mater.* **2021**, *11*, 2003405.
[10] T. R. Andersen, H. F. Dam, M. Hösel, M. Helgesen, J. E. Carlé, T. T. Larsen-Olsen, S. A. Gevorgyan, J. W. Andreasen, J. Adams, N. Li, F. Machui, G. D. Spyropoulos, T. Ameri, N. Lemaître, M. Legros, A. Scheel, D. Gaiser, K. Kreul, S. Berny, O. R. Lozman, S. Nordman, M. Välimäki, M. Vilkman, R. R. Søndergaard, M. Jørgensen, C. J. Brabec, F. C. Krebs, *Energy Environ. Sci.* **2014**, *7*, 2925.

[11] R. Søndergaard, M. Hösel, D. Angmo, T. T. Larsen-Olsen, F. C. Krebs, *Mater. Today* **2012**, *15*, 36.
[12] G. Zhang, K. Zhang, Q. Yin, X. F. Jiang, Z. Wang, J. Xin, W. Ma, H. Yan, F. Huang, Y. Cao, *J. Am. Chem. Soc.* **2017**, *139*, 2387.
[13] Z. Fu, J. W. Qiao, F. Z. Cui, W. Q. Zhang, L. H. Wang, P. Lu, H. Yin, X. Y. Du, W. Qin, X. T. Hao, *Adv. Mater.* **2024**, *36*, 2313532.
[14] H. Zhao, B. Lin, J. Xue, H. B. Naveed, C. Zhao, X. Zhou, K. Zhou, H. Wu, Y. Cai, D. Yun, Z. Tang, W. Ma, *Adv. Mater.* **2022**, *34*, 1.
[15] C. Xie, A. Classen, A. Späth, X. Tang, J. Min, M. Meyer, C. Zhang, N. Li, A. Osvet, R. H. Fink, C. J. Brabec, *Adv. Energy Mater.* **2018**, *8*, 1702857.
[16] L. Zhong, Z. Sun, S. Lee, S. Jeong, S. Jung, Y. Cho, J. Park, J. Park, S. J. Yoon, C. Yang, *Adv. Funct. Mater.* **2023**, *33*, 2305450.
[17] Y. Zhang, K. Liu, J. Huang, X. Xia, J. Cao, G. Zhao, P. W. K. Fong, Y. Zhu, F. Yan, Y. Yang, X. Lu, G. Li, *Nat. Commun.* **2021**, *12*, 4815.
[18] S. Luo, C. Li, J. Zhang, X. Zou, H. Zhao, K. Ding, H. Huang, J. Song, J. Yi, H. Yu, K. S. Wong, G. Zhang, H. Ade, W. Ma, H. Hu, Y. Sun, H. Yan, *Nat. Commun.* **2023**, *14*, 6964.
[19] L. Zhan, S. Li, X. Xia, Y. Li, X. Lu, L. Zuo, M. Shi, H. Chen, *Adv. Mater.* **2021**, *33*, 2007231.
[20] S. Lai, Y. Cui, Z. Chen, X. Xia, P. Zhu, S. Shan, L. Hu, X. Lu, H. Zhu, X. Liao, Y. Chen, *Adv. Mater.* **2024**, *36*, 2313105.
[21] W. Gao, F. Qi, Z. Peng, F. R. Lin, K. Jiang, C. Zhong, W. Kaminsky, Z. Guan, C. S. Lee, T. J. Marks, H. Ade, A. K. Y. Jen, *Adv. Mater.* **2022**, *34*, 2202089.
[22] C. Xie, X. Zeng, C. Li, X. Sun, S. Liang, H. Huang, B. Deng, X. Wen, G. Zhang, P. You, C. Yang, Y. Han, S. Li, G. Lu, H. Hu, N. Li, Y. Chen, *Energy Environ. Sci.* **2024**, *17*, 2441.
[23] C. Xie, H. Huang, Z. Li, X. Zeng, B. Deng, C. Li, G. Zhang, S. Li, *Polymers* **2024**, *16*, 91.
[24] C. Xie, S. Liang, G. Zhang, S. Li, *Polymers* **2022**, *14*, 4229.
[25] C. Xie, T. Heumüller, W. Gruber, X. Tang, A. Classen, I. Schuldes, M. Bidwell, A. Späth, R. H. Fink, T. Unruh, I. McCulloch, N. Li, C. J. Brabec, *Nat. Commun.* **2018**, *9*, 5335.
[26] J. Cho, S. Yoon, K. Min Sim, Y. Jin Jeong, C. Eon Park, S. K. Kwon, Y. H. Kim, D. S. Chung, *Energy Environ. Sci.* **2017**, *10*, 2324.
[27] A. Holmes, H. Laval, M. Guizzardi, V. Maruzzo, G. Folpini, N. Barbero, E. Deniau, M. Schmutz, S. Blanc, A. Petrozza, G. M. Paternò, G. Wantz, S. Chambon, C. Lartigau-Dagron, A. Bousquet, *Energy Environ. Sci.* **2024**, *17*, 1107.
[28] Z. Liu, C. Xie, T. Heumueller, I. McCulloch, C. J. Brabec, F. Huang, Y. Cao, N. Li, *Energy Environ. Sci.* **2025**, *18*, 155.
[29] X. Zeng, T. Xu, H. Chen, B. Deng, Q. Yan, X. Wen, Z. Li, H. Zeng, C. Gao, Y. Xiao, J. Liao, H. Liu, B. He, P. Han, G. Zhang, S. Li, Y. Chen, C. Xie, *Energy Environ. Sci.* **2024**, *17*, 9383.
[30] L. Wang, C. Chen, Y. Fu, C. Guo, D. Li, J. Cheng, W. Sun, Z. Gan, Y. Sun, B. Zhou, C. Liu, D. Liu, W. Li, T. Wang, *Nat. Energy* **2024**, *9*, 208.
[31] H. Hu, S. Liu, J. Xu, R. Ma, Z. Peng, T. A. Dela Peña, Y. Cui, W. Liang, X. Zhou, S. Luo, H. Yu, M. Li, J. Wu, S. Chen, G. Li, Y. Chen, *Angew. Chemie - Int. Ed.* **2024**, *63*, 202400086.
[32] H. Huang, G. Zhang, C. Xie, Z. Li, Q. Bai, B. He, M. Qiu, P. Han, H. Hu, S. Li, G. Zhang, *Adv. Funct. Mater.* **2025**, *35*, 2414844.
[33] D. Jiang, D. Wang, M. Chen, G. Zhou, Z. X. Liu, X. Li, H. Zhu, H. Li, H. Chen, C. Z. Li, *ACS Energy Lett.* **2022**, *7*, 1764.
[34] A. D. Scaccabarozzi, A. Basu, F. Aniés, J. Liu, O. Zapata-Arteaga, R. Warren, Y. Firdaus, M. I. Nugraha, Y. Lin, M. Campoy-Quiles, N. Koch, C. Müller, L. Tsetseris, M. Heeney, T. D. Anthopoulos, *Chem. Rev.* **2022**, *122*, 4420.
[35] F. Xue, Y. Xie, Y. Cui, D. Yu Paraschuk, W. Ma, H. Yan, *Adv. Funct. Mater.* **2024**, *35*, 2415617.
[36] Y. Cai, Q. Li, G. Lu, H. S. Ryu, Y. Li, H. Jin, Z. Chen, Z. Tang, G. Lu, X. Hao, H. Y. Woo, C. Zhang, Y. Sun, *Nat. Commun.* **2022**, *13*, 2369.
[37] L. J. A. Koster, V. D. Mihailetchi, R. Ramaker, P. W. M. Blom, *Appl. Phys. Lett.* **2005**, *86*, 123509.
[38] Y. Lin, Y. Firdaus, M. I. Nugraha, F. Liu, S. Karuthedath, A. H. Emwas, W. Zhang, A. Seitkhan, M. Neophytou, H. Faber, E. Yengel, I. McCulloch, L. Tsetseris, F. Laquai, T. D. Anthopoulos, *Adv. Sci.* **2020**, *7*, 1903419.
[39] H. Meng, C. Liao, M. Deng, X. Xu, L. Yu, Q. Peng, *Angew. Chemie* **2021**, *133*, 22728.
[40] B. Ray, A. G. Baradwaj, M. R. Khan, B. W. Boudouris, M. A. Alam, *Proc. Natl. Acad. Sci. USA* **2015**, *112*, 11193.
[41] H. Song, D. Hu, J. Lv, S. Lu, C. Haiyan, Z. Kan, *Adv. Sci.* **2022**, *9*, 2105575.
[42] H. S. Pang, H. Xu, C. Tang, L. K. Meng, Y. Ding, J. Xiao, R. L. Liu, Z. Q. Pang, W. Huang, *Org. Electron.* **2019**, *65*, 275.
[43] R. Xu, Y. Jiang, F. Liu, G. Ran, K. Liu, W. Zhang, X. Zhu, *Adv. Mater.* **2024**, *36*, 2312101.
[44] C. Wöpke, C. Göhler, M. Saladina, X. Du, L. Nian, C. Greve, C. Zhu, K. M. Yallum, Y. J. Hofstetter, D. Becker-Koch, N. Li, T. Heumüller, I. Milekhin, D. R. T. Zahn, C. J. Brabec, N. Banerji, Y. Vaynzof, E. M. Herzig, R. C. I. MacKenzie, C. Deibel, *Nat. Commun.* **2022**, *13*, 3786.
[45] Y. Zhang, G. Cai, Y. Li, Z. Zhang, T. Li, X. Zuo, X. Lu, Y. Lin, *Adv. Mater.* **2021**, *33*, 2008134.
[46] H. Chen, Y. Zou, H. Liang, T. He, X. Xu, Y. Zhang, Z. Ma, J. Wang, M. Zhang, Q. Li, C. Li, G. Long, X. Wan, Z. Yao, Y. Chen, *Sci. China Chem.* **2022**, *65*, 1362.
[47] Y. Liu, L. Zuo, X. Shi, A. K. Y. Jen, D. S. Ginger, *ACS Energy Lett.* **2018**, *3*, 2396.
[48] M. Zhang, L. Zhu, T. Hao, G. Zhou, C. Qiu, Z. Zhao, N. Hartmann, B. Xiao, Y. Zou, W. Feng, H. Zhu, M. Zhang, Y. Zhang, Y. Li, T. P. Russell, F. Liu, *Adv. Mater.* **2021**, *33*, 2007177.
[49] H. Yan, J. Chen, K. Zhou, Y. Tang, X. Meng, X. Xu, W. Ma, *Adv. Energy Mater.* **2018**, *8*, 1703672.